Research Article | Vol. 27, No. 9 | 29 Apr 2019 | OPTICS EXPRESS 13031
Optics EXPRESS

Optical plasmon nanostrip probe as an effective ultrashort pulse delivery system

YEVHENII M. MOROZOV,[1,2] ANATOLIY S. LAPCHUK,[2] IVAN V. GORBOV,[2] SONG-LONG YAO,[1] AND ZI-CHUN LE[1,*]

[1]College of Science, Zhejiang University of Technology, 288 Liuhe Road, 310023 Hangzhou, China
[2]Institute for Information Recording of NAS of Ukraine, 2 Shpaka Street, 03113 Kiev, Ukraine
*lzc@zjut.edu.cn

Abstract: In this paper, we analyze the ultrafast temporal and spectral responses of optical fields in tapered and metalized optical fibers (MOFs) and optical plasmon nanostrip probes (NPs). Computational experiment shows that output pulses of the NPs are virtually unchanged in shape and duration for input pulses with a duration of >1 fs and are not sensitive to changes in the parameters of the probe (such as convergence angle and taper length), while local enhancement of the electric field intensity reaches 300 times at the NP apex. Compared with the NPs, MOFs lead to significant output pulse distortions, even for input pulses with a duration of 10 fs. In addition, the temporal response at the MOF apex is critically sensitive to changes in MOF parameters and cannot provide any significant local enhancement of the electric field. These findings reveal the high potential of optical plasmon nanostrip probes as an ultrashort pulse delivery system to nanometer-size areas and indicate that its usage can be promising for a wide variety of techniques studying ultrafast processes in nanoscopic volumes.

© 2019 Optical Society of America under the terms of the OSA Open Access Publishing Agreement

1. Introduction

Revealing local chemical information at the level of individual nanoobjects is important in physics, chemistry, biology, materials science, and medicine. This task is now a routine requirement in many laboratories employing techniques such as Raman spectroscopy [1–11]. In addition, modern broadband lasers are capable of producing femtosecond pulses [12–15], which can be used for the study of ultrafast processes and coherent dynamics in a large variety of systems. The current challenge in nanophotonics is combining nanoscale light spots (≤ 100 nm) and ultrashort pulses (≤ 50 fs), the area where ultrasmall meets ultrafast [16–22]. The reason for this is that the focus of ultrafast science is rapidly moving toward increasingly complex systems [17], such as multiphoton microscopy in membranes and cells, quantum networks in diamond, or excitonic coherence in photosynthesis. However, the task of disentangling the heterogeneous contributions to dynamics in such complex structures requires femtosecond time resolution to be accompanied by nanometer spatial excitation volumes. Despite extensive developments, this goal has yet to materialize. One of the major challenges in this area is to engineer and control the ultrafast response of a system, which is required to fully realize the potential of ultrafast nanophotonics in physical, biological, and chemical applications. In particular, advances in this area can help researchers around the world to gain a better and deeper understanding of ultra-fast processes at the level of single nanoparticles.

Recently, in the field of ultrafast science, great attention has been paid to apertureless probes [22–26] and stand-alone plasmonic nanoantennas. However, despite little evidence for pulse distortion as long as the pulse durations are on the order of 10 fs, schemes involving these structures are usually connected with high background noise [27,28] and offer useful signal detection only in the far-field regime, making correct interpretation of the signal more difficult [29,30]. In addition, the ultrafast temporal and spectral responses of such structures

#359562 https://doi.org/10.1364/OE.27.013031
Journal © 2019 Received 5 Feb 2019; revised 31 Mar 2019; accepted 10 Apr 2019; published 24 Apr 2019

Optics EXPRESS

are very sensitive to the geometrical and physical parameters variation [31]. Among aperture-type probes, tapered and metalized optical fibers (MOFs) are widely used to confine light into a nanometer-size spot [32–35]. This widespread utilization is related to their mature and relatively simple and cheap fabrication techniques. However, MOFs suffer from low optical efficiency (10^{-6}–10^{-3} at a tip diameter d of 100 nm), which leads to a small signal-to-noise ratio and the complexity of useful signal detecting. Additionally, because of the dispersion [36–38], cutoff core tip diameter [37], and ghost re-reflection from the metal coating, the signal can be significantly degraded and extended in time during travel through the MOF to the nanoscale tip apex. To increase optical efficiency, several structures have been proposed, among which an optical plasmon microstrip probe (other names include "metal-insulator-metal gap plasmon waveguide" and "campanile near-field probe") [39–45,30] is the most promising because of its relatively high optical efficiency (2×10^{-1} at d = 30 nm) and high electric field intensity enhancement (up to 2500 at the probe apex). The name "microstrip probe" originates from microwave theory; in fact, this structure has nanometer characteristic sizes. Thus, in this paper, we use the name "optical plasmon nanostrip probe" (OPNP, or just NP), because such a name reflects the physical reality of this structure more correctly. At the same time, Lapchuk et al. showed [40] that the fundamental quasi-TM_{00} mode of the NP has no dispersion, which can indicate that an ultrashort pulse will not be significantly extended in time during propagation down to the probe nanoscale apex. In addition, this fundamental mode does not have a cutoff frequency, which allows its propagation down to the subwavelength tip apex and formation of a 10–50 nm highly intensive light spot without noticeable re-reflection from the metallic coatings. All of these characteristics make application of the nanostrip probe as an ultrashort pulse delivery system to nanometer-size areas very promising in a wide variety of techniques studying ultrafast processes, such as femtosecond-stimulated Raman spectroscopy [46–52] and femtosecond time-resolved impulsive stimulated Raman spectroscopy [53,54].

Because, to the best of our knowledge, the abovementioned structures (metalized optical fibers and optical plasmon nanostrip probes) have not been considered for this purpose, neither theoretically nor experimentally, we provide in this paper a computational experiment on the propagation of ultrashort pulses (< 10 fs at the FWHM intensity level) in MOFs and NPs and confirm the assumption regarding the potential of the nanostrip probe as an ultrashort pulse delivery system. Along with recently proposed methods for the manufacture and effective excitation of the NP [45,55], these findings may give a new impetus to the development of ultrafast nanophotonics.

2. Details of numerical simulation

The analysis was based on the numerical solution of linear Maxwell's equations by the three-dimensional finite-difference time-domain method [56]. The Drude model [57] was used to describe the interaction of the metals with electromagnetic radiation. The parameters of the employed materials were taken from [58]. We used the Drude model and multi-coefficient model [59] to fit the dielectric functions of gold and fused silica, respectively. Despite the fact that interband absorption plays an important role on the femtosecond scale [60], utilizing of the Drude model for structures analyzed in the manuscript is appropriate for the following reasons: 1) In the case of MOFs, propagating modes considered in the manuscript almost do not penetrate in the metal and energy losses are mainly due to their back reflection from the metal coating, rather than absorption in the metal. Absorption plays more important role at the very tip of the MOFs (where the tip diameter is relatively small), however most of the modes in this area are cutoff and, therefore, length of this absorption area is too short to make a significant influence on the obtained output signals. 2) In the case of NPs, if excitation photon energy is higher than the threshold for interband transition in a metal, interband electrons excitation may lead to additional intensity attenuation [61] of the fundamental plasmon mode of the NP, however qualitatively it will not change the obtained output signals. All boundaries

Optics EXPRESS

of the simulation cube contained perfectly matched layers and were set to be more than 400 nm away from the surfaces of the metal structure to avoid absorption of near fields. The magnetic wall was placed in the plane of symmetry, $y = 0$. The convergence of the numerical simulation results and the mesh adaptation of the models used were also analyzed before the simulation (see Appendix).

In Fig. 1, the initial MOF model used for simulation is presented with its legend. Materials used: core – bare fused silica (cyan color); coating – gold (yellow color). Among other metals, gold was chosen based on the following criterion: $|\varepsilon_{imag}| << |\varepsilon_{real}|$, where ε_{imag} is the imaginary part and ε_{real} is the real part of the complex permittivity of the medium; it has relatively low dissipative losses at wavelengths above 550 nm. The diameter of the input coupler (4,000 nm) was chosen based on readily available single-mode fibers for wavelengths of 600-850 nm. The tip diameter d and convergence semi-angle α for the initial MOF configuration were 100 nm and 20.7°, respectively. The tip diameter d of 100 nm was chosen to achieve subwavelength spatial resolution. Convergence semi-angles for all MOF configurations were chosen according to readily available fabrication techniques [62–65]. It is worth to note here that since this structure is absolutely symmetrical with respect to the axis of rotation, the output signal is invariant with respect to the direction of linear polarization of the exciting laser radiation.

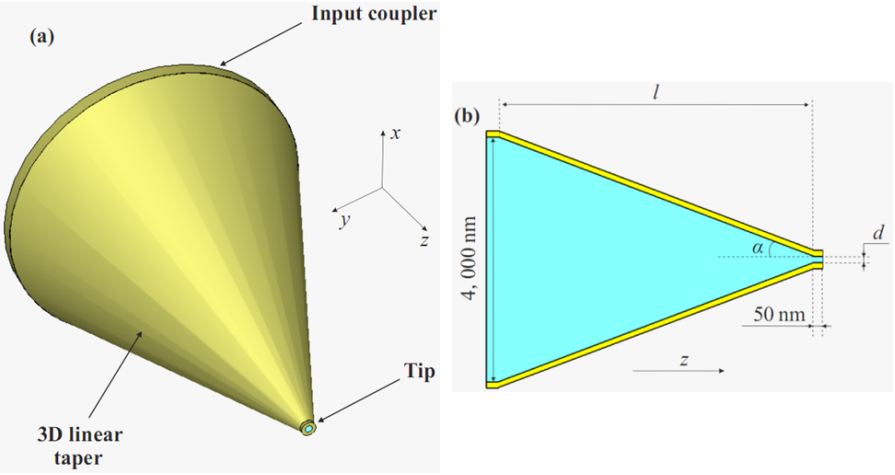

Fig. 1. Perspective (a) and cross-sectional side (b) views of a schematic illustration of a MOF structure: l is the length of the taper section; α is the convergence semi-angle; d is the tip apex diameter; the thickness of the gold coating is 50 nm.

As the skin depth of gold is approximately 25 nm at a wavelength of 833 nm, the thickness of the gold coating of 50 nm is sufficient to prevent any field penetration through the coating. To excite this structure, we used the TE_{11} mode of a regular perfect electrical conductor (PEC) waveguide filled with fused silica. This excitation method was dictated by the desire to excite mostly the guided HE_{11} mode of the MOF, as among other guided modes, this mode has the smallest cutoff diameter and thus is the most preferable one in a real experiment.

In Fig. 2, the initial NP model used for simulation with its legend is illustrated. Materials used: core – bare fused silica (cyan color); covering strips – gold (yellow color). The convergence angle α for the initial NP configuration was 46.4°. The parameters of the NP were chosen according to the fabricated nanodevice [43]. It is worth to note here that linear x-polarized exciting laser radiation is required for this structure, because in the case of polarization along y-axis, the excited mode of NP will be characterized by a very small throughput due to the cutoff frequency and high background noise, which makes this case uninteresting from the application point of view.

Optics EXPRESS

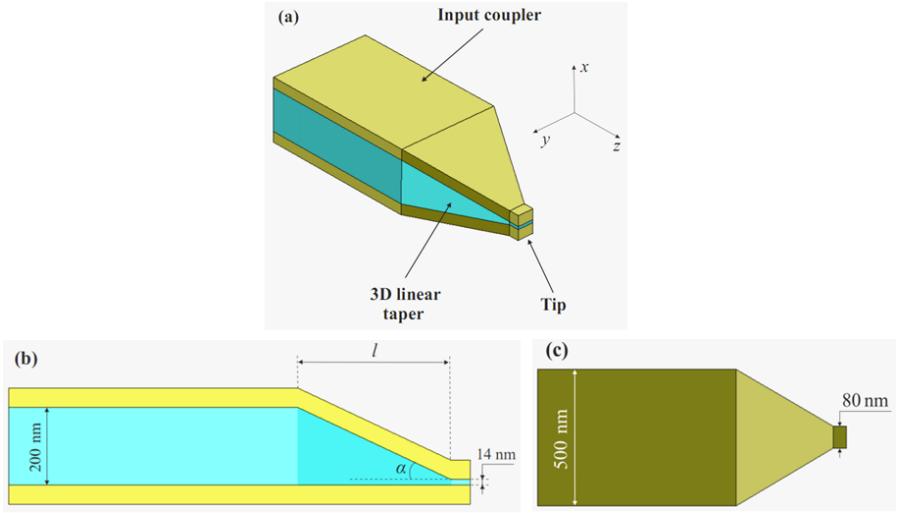

Fig. 2. Perspective (a), cross-sectional side (b), and top (c) views of a schematic illustration of the NP structure: l is the length of the taper section; α is the convergence angle; the thickness of the gold coating is 50 nm.

The electric field of the electromagnetic wave of a pulse produced by an ultrafast laser can be expressed in the following form [12]

$$E^{input}(t) = A(t)\sin(\omega_0 t + \varphi), \tag{1}$$

where $A(t)$ is the pulse shape envelope, ω_0 is the carrier frequency of the center of the laser emission spectrum, and φ is the phase offset between the envelope maximum and the nearest maximum of the carrier frequency. The appearance of a phase offset is related to the fact that the envelope moves at the group velocity, while the carrier frequency moves at the phase velocity; because of dispersion in the resonator, these velocities are different. In our simulation, to excite the structures under consideration, we used three ultrashort Gaussian-shaped pulses centered at 833 nm (f_0 = 3.6e14 Hz) with different FWHM duration times Δt (see Fig. 3): 0.79 (a), 4.33 (b), and 9.45 (c) fs. Note unless otherwise specified, all intensities in the paper are normalized to the maximum value of the input pulse intensities.

Linear optical transmission through a structure is fully characterized by the complex-valued transfer function $Z(\omega)$ in the following form [66]:

$$E^{output}(\omega) = Z(\omega)E^{input}(\omega), \tag{2}$$

where $E^{input}(\omega)$ and $E^{output}(\omega)$ are respectively the source field and the corresponding response of the structure in the frequency domain. In this way, knowledge of the transfer function $Z(\omega)$ and $E^{input}(\omega)$ makes it possible to calculate the output signal $E^{output}(t)$ in the time domain. However, transfer function does not provide visual information about the shape and duration of the output signal, so for clarity in the paper we presented the transfer function via the input and output signals.

Optics EXPRESS

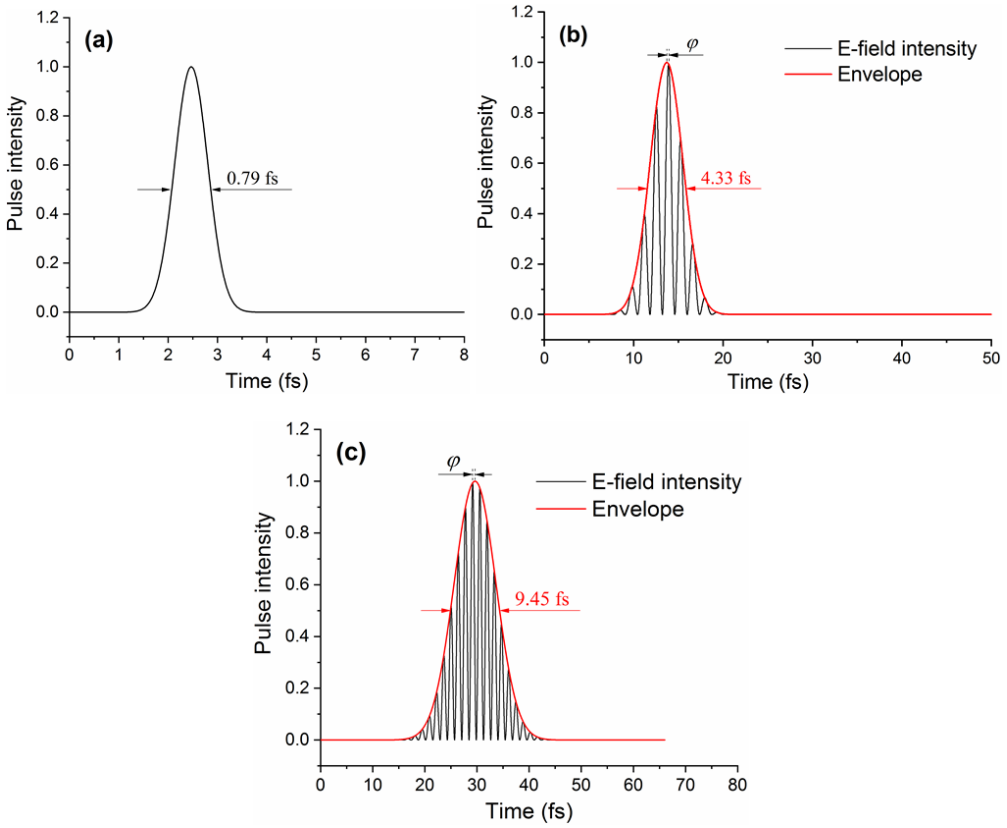

Fig. 3. Ultrashort Gaussian-shaped pulses centered at 833 nm (f_0 = 3.6e14 Hz) with different duration times Δt: 0.79 (a), 4.33 (b), and 9.45 (c) fs.

In the next Section, we will present results showing the evolution of the pulses as they propagate to the tip apex of the probes for various probe configurations.

3. Results and discussion

3.1. Tapered and metalized optical fibers

Figure 4(a) shows the signal intensity envelopes (excitation laser pulse duration Δt = 0.79 fs) at the start of the input coupler and at the very end (at the apex) of the MOF for the initial { + Au}{ + tip} configuration (red curve); modified {-Au}{ + tip} configuration without gold coating of the tip (green curve); and modified{-Au}{-tip} configuration without a 50-nm tip at all (blue curve). For the { + Au}{ + tip} configuration (Fig. 4(a), red curve), the output signal first peak intensity is 0.055 and the second one is 0.078. Local field attenuation for the first peak is 18.2 times. The duration of the first peak is 2.76 fs (absolute elongation is 1.97 fs; relative elongation is 249.4%), and that of the second one is 2.16 fs (absolute elongation is 1.37 fs; relative elongation is 173.4%). The time delay between the input signal and the first peak of the output signal is 30.85 fs.

Optics EXPRESS

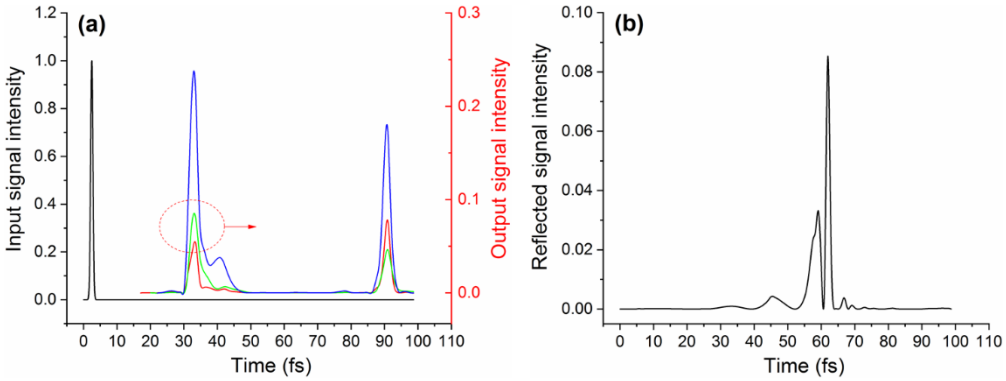

Fig. 4. (a) Signal intensity envelopes at the start of the input coupler and at the very end of the MOF for the initial { + Au}{ + tip} configuration (red curve); modified {-Au}{ + tip} configuration without gold coating of the tip (green curve); and modified {-Au}{-tip} configuration without a 50-nm tip at all (blue curve); (b) Reflected signal intensity at the start of the MOF for modified {-Au}{-tip} configuration. $\Delta t = 0.79$ fs; $\alpha = 20.7°$; $l = 5{,}161$ nm; $d = 100$ nm.

For the {-Au}{ + tip} configuration (Fig. 4(a), green curve), the output signal first peak intensity is 0.085 and that of the second one is 0.046. Local field attenuation for the first peak is 11.8 times. The duration of the first peak is 2.99 fs (absolute elongation is 2.20 fs; relative elongation is 278.5%), and that of the second one is 2.89 fs (absolute elongation is 2.20 fs; relative elongation is 265.8%). In this case, the first peak is higher than the second one (compare with the red curve). The time delay between the input signal and the first peak of the output signal is 30.63 fs.

For the {-Au}{-tip} configuration (Fig. 4(a), blue curve), the output signal first peak intensity is 0.238 and that of the second one is 0.180. Local field attenuation for the first peak is 4.2 times. The duration of the first peak is 2.86 fs (absolute elongation is 2.07 fs; relative elongation is 262.0%), and that of the second one is 2.53 fs (absolute elongation is 1.74 fs; relative elongation is 220.3%). In this case, the first peak is also higher than the second one, but has a much larger intensity than for {-Au}{ + tip}. The appearance of the input signal peak is observed at 2.47 fs; that of the output signal first peak at 33.01 fs; and that of the second peak at 90.73 fs. Thus, the time delay between the input signal and the first peak of the output signal is 30.54 fs, and that between the first peak and the second peak of the output signal is 57.72 fs. In this way, the second peak of the output signal for all configurations can be explained by the multiple reflections of the electromagnetic waves from the metallic coating of the MOF. To confirm this, we measured the reflected signal intensity at the start of the input coupler for the modified {-Au}{-tip} configuration. The reflected signal intensity is illustrated in Fig. 4(b). The reflected peak with the highest intensity is observed at 61.99 fs, which confirms our assumption about multiple re-reflection of the pulse.

In the first approximation, we can consider the light propagation in a MOF as separate modes propagating in a tapering cylindrical waveguide with a dielectric core and metal layer cladding. A set of different modes arise at the interface between a common waveguide (dielectric waveguide or dielectric waveguide with perfect metal cladding, as in our case) and a plasmon cylindrical waveguide because of the different electric field structures of the modes of these waveguides. Because the MOF structure has cylindrical symmetry, a beam should preserve the symmetry of the excitation mode and only modes with azimuthal index “1” should be taken into account. As the tapering waveguide is an inhomogeneous one, there is thus an effect of mode transformation. However, because the different modes have a very different field structure and the change in waveguide shape with light propagation is relatively slow, in the first approximation we can neglect the effect of mode interaction. In

Optics EXPRESS

this case, the main effect of waveguide tapering will be a mode back-reflection on the way to the probe apex and practically full back-reflection when they reach their cutoff size.

The dispersion of modes in a cylindrical waveguide with a dielectric core and finite metal cladding was analyzed in much detail in [37,38]. Below, we will use the mode classification proposed by Novotny and Hafner in [37]. Because all modes with azimuthal index "1" (except HE_1) have cutoff diameters, only several first modes having the smallest cutoff diameter play an important role in energy transmission to the MOF apex. For small MOF diameters, the HE_1 mode mostly propagates outside the waveguide area [37] and therefore will not be excited under our excitation condition, so it can be omitted from the analysis. Hence, the HE_{11}, EH_{11}, HE_{12}, and EH_{12} modes play the main role in energy transmission to the MOF apex, and the most important are the first two modes. All first modes with azimuthal index "1" have strong dispersion in the diameter range close to that of the cutoff. This results in beam width broadening for every waveguide mode and a shift in time of the beams of different modes. The time and phase shifts of the different waveguide modes beams result in interference of fields at the MOF apex. The first output energy pulse has two definite subpeaks that can be associated with the two beams of the HE_{11} and EH_{11} modes (see Fig. 4(a)). The result of the strong laser beam intensity peak extension is a small intensity of light at the probe apex. The second output pulse is due to the re-reflection and returning back beam. The reflected back beam is clearly seen in Fig. 4(b). The reflected signal has a more complicated shape because it is the interference of many reflected-back waveguide modes. In all three cases depicted in Fig. 4(a), the second peak of the output signal is less distorted than the first one; however, as a result of the comparison of intensity with the first peak, it should be an in-phase interference of the fields of two modes. From Fig. 4(a), it is obvious that the {-Au}{-tip} configuration is the most suitable for application because it provides the highest signal intensity at the end of the MOF.

Figure 5 shows the input and output signal intensity envelopes (Figs. 5(a) and 5(c)) and signal amplitudes (Figs. 5(b) and 5(d)) for the {-Au}{-tip} configuration of the MOF for (Figs. 5(a) and 5(b)) pulse duration $\Delta t = 4.33$ fs and (Figs. 5(c) and 5(d)) $\Delta t = 9.45$ fs.

From Fig. 5(a) {$\Delta t = 4.33$ fs}, the output signal first peak intensity is 1.918, that of the second one is 0.882, that of the third one is 0.139, and that of the fourth one is 0.085. Local field enhancement for the first peak is 1.9 times. The duration of the first peak is 7.77 fs (absolute elongation is 3.44 fs; relative elongation is 79.4%), that of the second is 5.14 fs (absolute elongation is 0.81 fs; relative elongation is 18.7%), that of the third is 6.06 fs (absolute elongation is 1.73 fs; relative elongation is 40.0%), and that of the fourth is 4.87 fs (absolute elongation is 0.54 fs; relative elongation is 12.5%). The time delay between the input signal and the first peak of the output signal is 31.12 fs.

From Fig. 5(c) {$\Delta t = 9.45$ fs}, the output signal first peak intensity is 3.412, that of the second one is 0.748, and that of the third one is 0.207. Local field enhancement for the first peak is 3.4 times. The duration of the first peak is 12.36 fs (absolute elongation is 2.91 fs; relative elongation is 30.8%), that of the second is 8.99 fs (absolute compression is 0.46 fs; relative compression is 4.9%), and that of the third is 11.06 fs (absolute elongation is 1.61 fs; relative elongation is 17.0%). The time delay between the input signal and the first peak of the output signal is 32.58 fs.

From Figs. 4 and 5, it is clear that fs pulses significantly degrade during propagation through a MOF to its subwavelength apex. In addition, local field enhancement is not pronounced (< 4 times), and for a pulse with $\Delta t = 0.79$ fs, even attenuations up to 18.2 times were observed (see Fig. 4(a)). The decrease in field enhancement with the decrease in initial pulse duration can be easily explained by a large pulse elongation at the probe apex for shorter pulses.

Optics EXPRESS

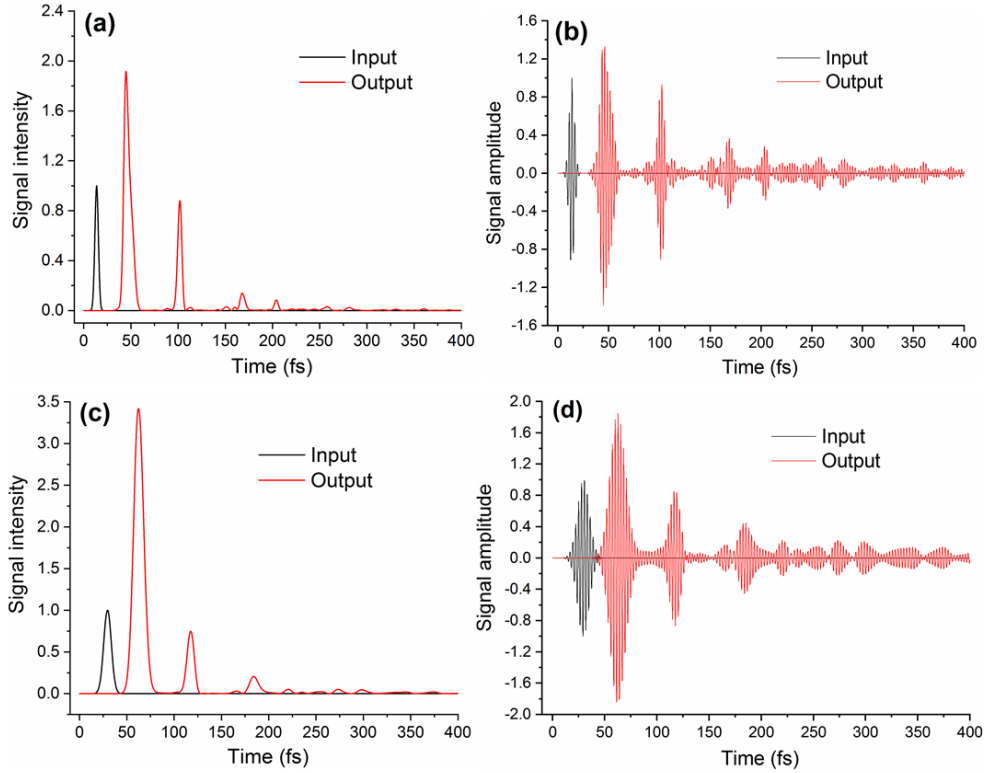

Fig. 5. Input and output signal intensity envelopes (a,c) and signal amplitudes (b,d) of the MOF for the {-Au}{-tip} configuration for (a,b) pulse duration $\Delta t = 4.33$ fs and (c,d) $\Delta t = 9.45$ fs. $\alpha = 20.7°$; $l = 5{,}161$ nm; $d = 100$ nm.

It is well known that very weak field enhancement (and even significant attenuation in some cases) can be attributed to the cutoff diameter of the MOF apex (d = 100 nm; $d_{\text{cutoff}} \sim \lambda_0/2 \cdot \text{sqrt}(n) \approx 300$ nm), where all guided modes become attenuated. To demonstrate this fact, we performed simulation for apex diameters d of 400 and 600 nm for a pulse width $\Delta t = 0.79$ fs for the {-Au}{-tip} configuration (see Fig. 6(a)). Also in Fig. 6(a), the output signal intensity envelope for a taper that is twice as short (larger convergence semi-angle, $\alpha = 37.1°$; $l = 2{,}580.5$ nm) with $d = 100$ nm is shown (blue curve).

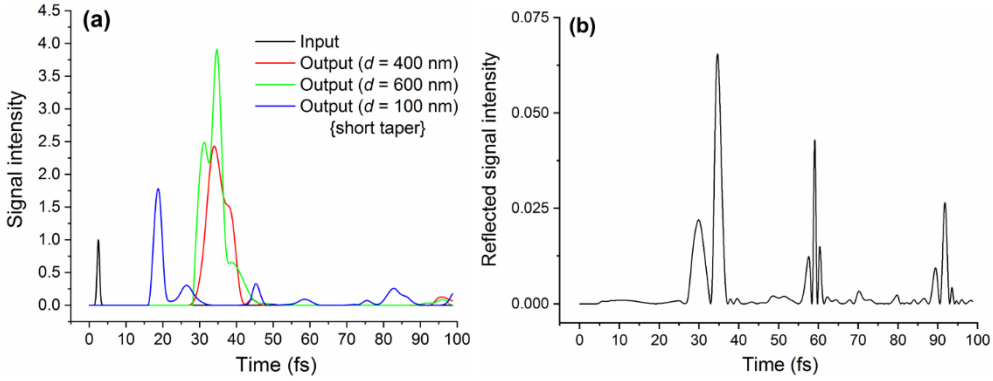

Fig. 6. (a) Signal intensity envelopes for the {-Au}{-tip} configuration with $d = 400$ nm, $\alpha = 20.7°$ (red curve); $d = 600$ nm, $\alpha = 20.7°$ (green curve); and $d = 100$ nm, $\alpha = 37.1°$ (blue curve); (b) Reflected signal intensity at the start of the MOF for modified short taper configuration: $\Delta t = 0.79$ fs; $\alpha = 37.1°$; $l = 2{,}580.5$ nm; $d = 100$ nm.

Optics EXPRESS

For d = 400 nm, α = 20.7° (Fig. 6(a), red curve), the output signal first peak intensity is 2.432; that of the second one is 0.127. Local field enhancement for the first peak is 2.4 times. The duration of the first peak is 7.54 fs (absolute elongation is 6.75 fs; relative elongation is 854.4%); that of the second is 5.04 fs (absolute elongation is 4.25 fs; relative elongation is 538.0%). In this case, despite the much higher intensity of the output signal first peak, the peak is significantly stretched in time. The time delay between the input signal peak and the first peak of the output signal is 31.51 fs.

For d = 600 nm, α = 20.7° (Fig. 6(a), green curve), the output signal first peak intensity is 3.920; that of the second one is 0.087. Local field enhancement for the first peak is 3.9 times. The duration of the first peak is 6.31 fs (absolute elongation is 5.52 fs; relative elongation is 698.7%); that of the second one is 3.43 fs (absolute elongation is 2.64 fs; relative elongation is 334.2%). Therefore, in the case of d = 600 nm, despite the much higher intensity of the first peak of the output signal, the peak is also significantly stretched in time. The time delay between the initial signal and the first peak of the output signal is 32.21 fs. In this case, we can also see an additional subpeak at 31.2 fs before the main subpeak at 34.7 fs. This additional subpeak can be attributed to the guided HE_{12} mode [37]. At d = 400 nm, this guided HE_{12} mode is rapidly attenuated and cannot be seen in the red curve (see Fig. 6(a)).

For a short taper, d = 100 nm, α = 37.1° (Fig. 6(a), blue curve), the output signal first peak intensity is 1.781; that of the second one is 0.329; and that of the third one is 0.259. Local field enhancement for the first peak is 1.8 times (in this case, we even obtain the field enhancement, not attenuation as for the initial taper with d = 100 nm, which can be explained by the shorter "cutoff" taper length). The duration of the first peak is 2.59 fs (absolute elongation is 1.80 fs; relative elongation is 227.8%); that of the second one is 2.32 fs (absolute elongation is 1.53 fs; relative elongation is 193.7%); and that of the third one is 5.63 fs (absolute elongation is 4.84 fs; relative elongation is 612.7%). The time delay between the initial signal and the first peak of the output signal is 16.24 fs. It is worth noting that for this configuration, the second peak is not as intense as it was for the initial taper (see Fig. 4(a), blue curve). Figure 6(b) shows the reflected signal intensity at the probe start for a short taper. In Fig. 6(b), a few peaks can be observed, which also indicates the multiple reflection of the pulse in the MOF.

Summing up these results, we can conclude that, using a MOF, it is impossible to achieve a single-peak not-extended response at the probe apex because of the significant pulse distortion during propagation. In addition, the output signal shape is very sensitive to the structure configuration, which means that it is difficult for this structure to control the output signal. All this requires an in-depth preliminary engineering work, for instance, the use of different laser pulse shaping techniques [67–69]. Thus, this structure requires very careful manufacturing with high reproducibility.

In Fig. 7, the spectral dependence of the input and output signals of the {-Au}{-tip} configuration of the MOF with an initial taper (α = 20.7°; l = 5,161 nm) is shown for initial pulse durations Δt of (a) 0.79 fs, (b) 4.33 fs, and (c) 9.45 fs for d = 100 nm. Also, in Fig. 7(a), the output signal of the MOF {-Au}{-tip} configuration with a shorter taper (α = 37.1°; l = 2,580.5 nm) is illustrated (green curve). From Fig. 7(a), it is clear that the output signal intensity is slightly higher only in the frequency range of 350 to 620 THz. Under 350 THz, the output signal is lower than the input one and reduces as the frequency approaches 0. This result can be explained by the fact that, for the same MOF cross-section diameter, lower frequencies are reflected more strongly. A small drop after 500 THz can be attributed to the increased losses in the gold cladding starting at these frequencies. Thus, the intensity distribution of the output signal is irregular. Note that knowledge of $E^{input}(\omega)$ and $E^{output}(\omega)$ gives the ability to calculate the so-called impulse response function [67] and, therefore, to perform a necessary laser pulse shaping.

Optics EXPRESS

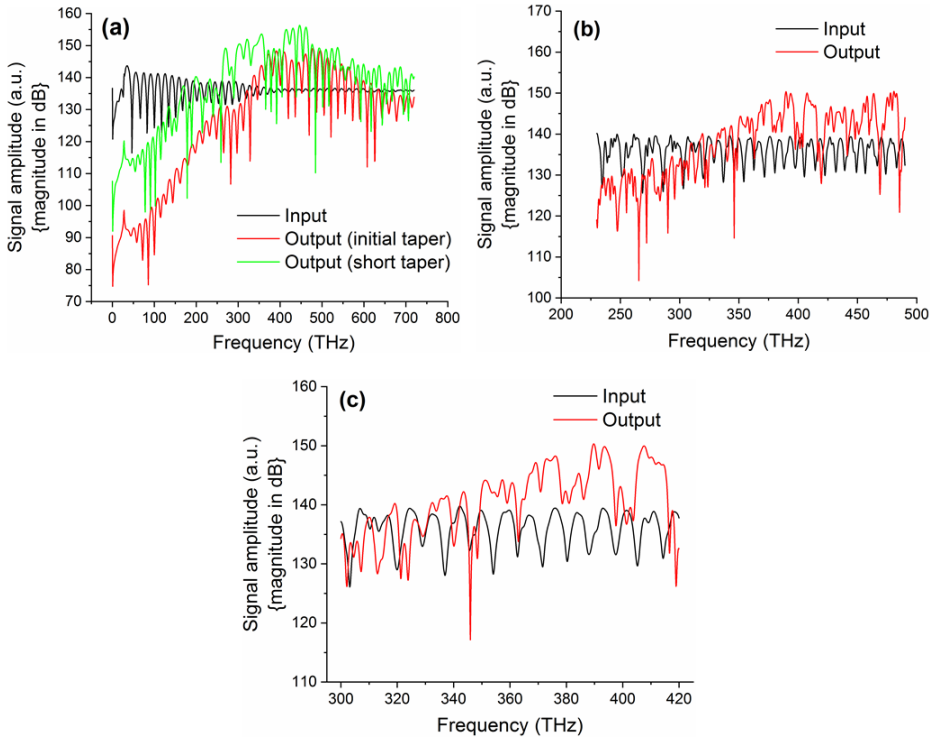

Fig. 7. The spectral dependence of the output signal of the MOF for initial pulse durations Δt of (a) 0.79 fs, (b) 4.33 fs, and (c) 9.45 fs; {-Au}{-tip} configuration; d = 100 nm. Note: here amplitudes are not normalized to the maximum input value.

3.2. Optical plasmon nanostrip probe

Figure 8 shows the signal intensity envelopes (excitation laser pulse duration Δt = 0.79) at the start of the input coupler (black curve) and at the very end (at the apex) of the NP for the initial { + tip} configuration (red curve); modified {-tip} configuration without tip (pink curve); modified fully symmetric {sym} configuration without tip (blue curve) (convergence semi-angle, α = 49.0°); and for a taper that is 2.75 times longer (lower convergence angle, α = 20.9°) {long_taper} (black dashed curve).

For the { + tip} configuration (Fig. 8, red curve), the output signal peak intensity is 169.474. Local field enhancement for the output peak is 169.5 times. The duration of the output peak is 1.42 fs (absolute elongation is 0.63 fs; relative elongation is 79.7%). The time delay between the input signal peak and the peak of the output signal is 8.30 fs.

For the {-tip} configuration (Fig. 8, pink curve), the output signal peak intensity is 194.035. Local field enhancement for the output peak is 194.0 times. The duration of the output peak is 1.43 fs (absolute elongation is 0.64 fs; relative elongation is 81.0%). The time delay between the input signal peak and the peak of the output signal is 7.43 fs. Thus, as the length of the tip decreases (or in the case of its absence), the output signal peak increases in intensity, which coincides with the results obtained in [43].

For the {sym} configuration (Fig. 8, blue curve), the output signal peak intensity is 204.561. Local field enhancement for the output signal peak is 204.6 times. The duration of the output peak is 1.42 fs (absolute elongation is 0.63 fs; relative elongation is 79.7%). The time delay between the input signal peak and the peak of the output signal is 7.73 fs. Figure 8 shows that the fully symmetric configuration of the NP without a tip has the highest output signal intensity.

Optics EXPRESS

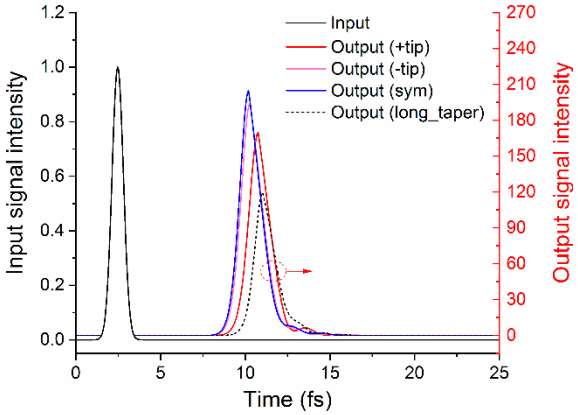

Fig. 8. Signal intensity envelopes (excitation laser pulse duration $\Delta t = 0.79$) at the start (black curve) and at the end of the NP for the initial { + tip} configuration (red curve); modified {-tip} configuration without tip (pink curve); modified fully symmetric {sym} configuration without tip (blue curve); and for a taper that is 2.75 times longer (lower convergence semi-angle, $\alpha = 20.9°$) {long_taper} (black dashed curve).

For the {long_taper} configuration (Fig. 8, black dashed curve), the output signal peak intensity is 119.649. Local field enhancement for the end peak is 119.6 times. The duration of the output signal peak is 1.35 fs (absolute elongation is 0.59 fs; relative elongation is 70.9%). The time delay between the input signal peak and the peak of the output signal is 8.17 fs. It is interesting to note that in the case of the NP, increasing the taper length from 400 to 1,100 nm does not lead to a significant increase in the time delay (the increase is approximately 0.75 fs). However, in the case of the MOF, increasing the taper length from 2,580.5 to 5,161 nm leads to an increase in the time delay of 14.31 fs.

Figure 9 shows the input and output signal intensity envelopes (Figs. 9(a) and 9(c)) and signal amplitudes (with envelopes) (Figs. 9(b) and 9(d)) at the start and end of the NP for the {-tip}{initial taper} configuration for (Figs. 9(a) and 9(b)) pulse durations $\Delta t = 4.33$ fs and (Figs. 9(c) and 9(d)) $\Delta t = 9.45$ fs.

From Fig. 9(a) {$\Delta t = 4.33$ fs}, the output signal peak intensity is 278.095. Local field enhancement for the output signal peak is 278.1 times. The duration of the output signal peak is 4.43 fs (absolute elongation is 0.10 fs; relative elongation is 2.3%). The time delay between the input signal peak and the peak of the output signal is 8.52 fs.

From Fig. 9(c) {$\Delta t = 9.45$ fs}, the output signal peak intensity is 305.980. Local field enhancement for the output signal peak is 306.0 times. The duration of the output signal peak is 9.65 fs (absolute elongation is 0.20 fs; relative elongation is 2.1%). The time delay between the input signal peak and the peak of the output signal is 8.64 fs.

From Figs. 8 and 9, it is obvious that fs pulses degrade insignificantly during propagation through the NP to its subwavelength apex. In addition, local field enhancement is relatively noticeable (up to 306 times). Note that for all NP configurations, the time delay between the input signal peak and the peak of the output signal is no longer than 9 fs, which makes the NP suitable for use as a simultaneous pump and probe pulse delivery system.

Summing up these results, we conclude that using the NP for pulses with duration $\Delta t > 4$ fs does not lead to any noticeable pulse degradation and allows a single-peak not-extended response with enhanced intensity at the probe apex. At the same time, for a pulse with $\Delta t < 1$ fs, a slight output pulse extension is observed; however, the output signal has only one peak, which preserves the virtually ideal Gaussian shape. Additionally, the output signal shape is insensitive to changes in the structure configuration for all pulses, which means that it is easy for this structure to control the output signal and it does not require in-depth preliminary engineering work. Therefore, this structure does not require careful manufacturing with high reproducibility.

Optics EXPRESS

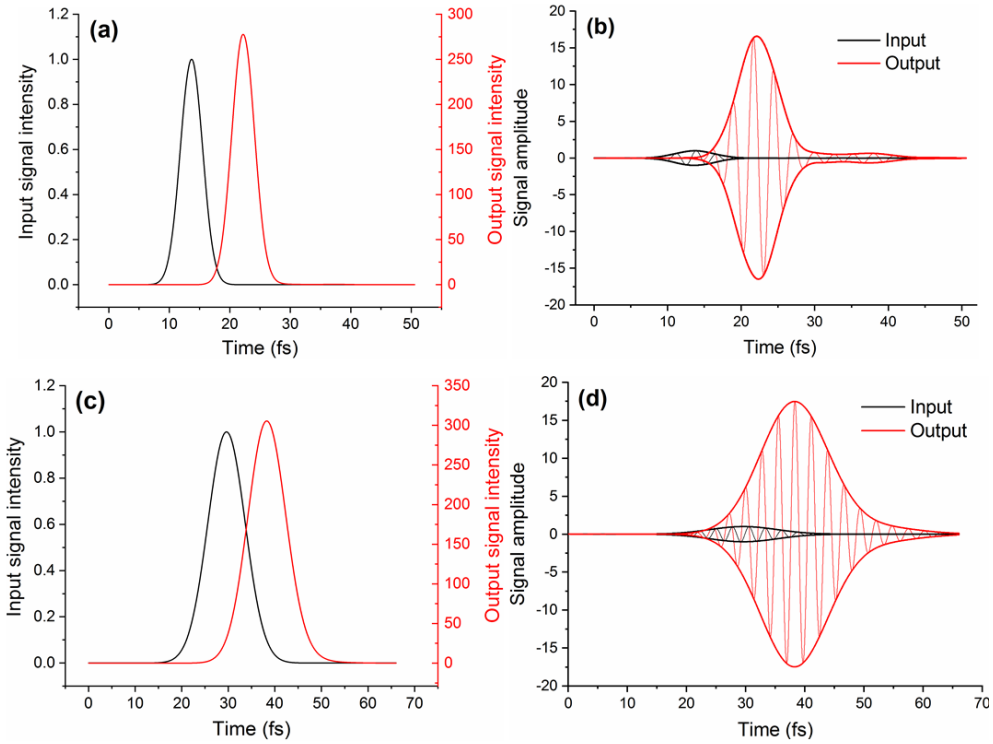

Fig. 9. Signal intensity envelopes (a,c) and signal amplitudes (with envelopes) (b,d) at the start and end of the NP for the {-tip}{initial taper} configuration for (a,b) pulse durations Δt = 4.33 fs and (c,d) Δt = 9.45 fs; α = 46.4°.

To compare both structures, in Fig. 10, only the output signal intensities are shown for the (a) MOF and (b) NP with different taper lengths. From Fig. 10, it is clear that the NP output signal is virtually unchanged, as only the intensity is slightly changed with a change in the taper angle. In comparison with the NP, the MOF output signal is significantly degraded and its shape also changes as the taper angle changes.

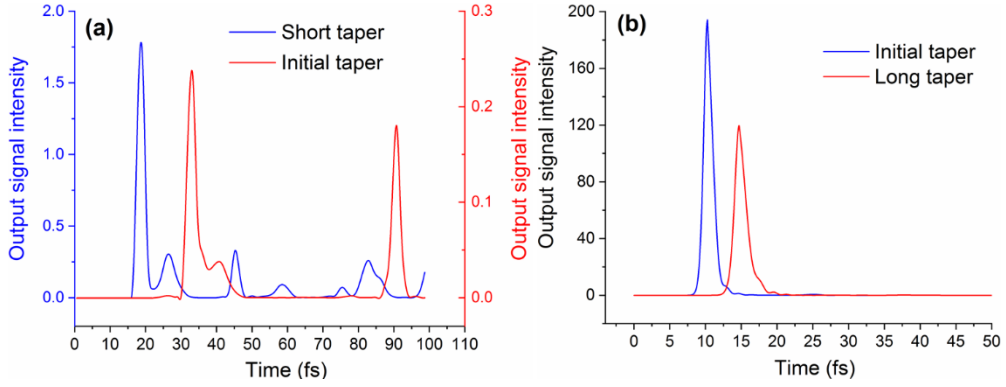

Fig. 10. Comparison of the MOF (a) and NP (b) for different convergence angles; Δt = 0.79 fs.

In Fig. 11, the spectral dependence of the input and output signals of the {-tip} configuration of the NP (α = 46.4°; l = 400 nm) is shown for initial pulse durations Δt of (a) 0.79 fs, (b) 4.33 fs, and (c) 9.45 fs. Also, in Fig. 11(a), the output signal of the NP {-tip} configuration with a longer taper (α = 20.9°; l = 1,100 nm) {green curve} is illustrated. From Fig. 11(a), it can be seen that the amplitude of the output signal is higher than for the input

Optics EXPRESS

one throughout the entire frequency range. Additionally, the amplitude distribution is virtually uniform, with a small drop above 500 THz. This drop can be attributed to increased loss in the gold stripes starting at these frequencies.

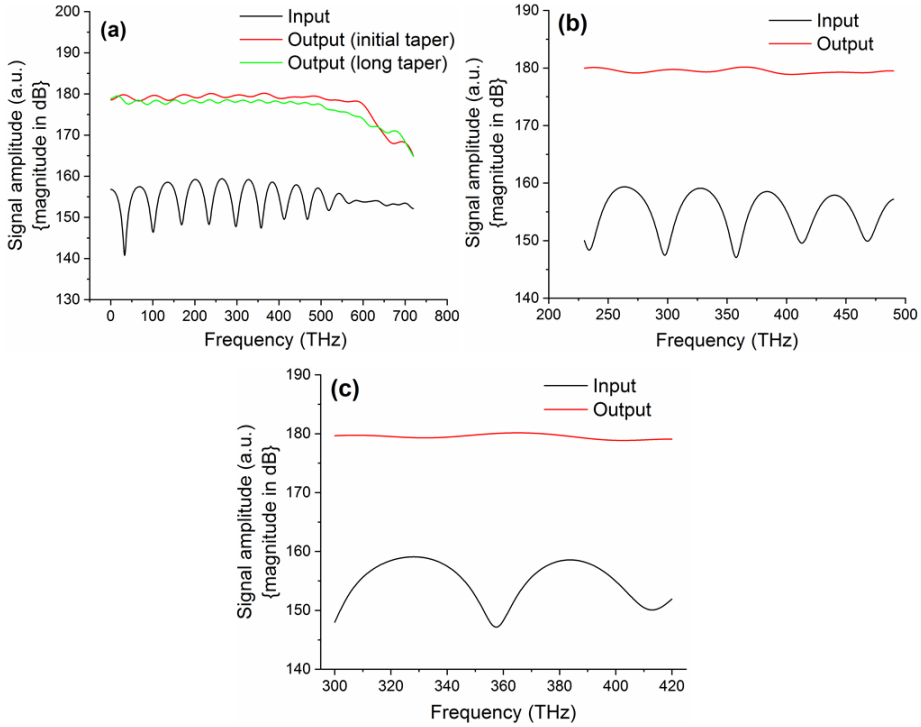

Fig. 11. The spectral dependence of the input and output signals of the NP for initial pulse durations Δt of (a) 0.79 fs, (b) 4.33 fs, and (c) 9.45 fs. Note: here amplitudes are not normalized to the maximum input value.

In Fig. 12, the dependence of the axial z-component of the output signal intensity of the MOF (black curve) and NP (red curve) is shown for an initial pulse duration Δt of 0.79 fs.

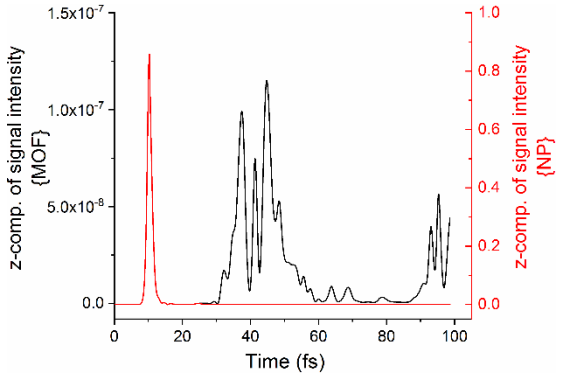

Fig. 12. Dependence of the axial z-component of the output signal intensity of the MOF (black curve) and NP (red curve) for an initial pulse duration Δt of 0.79 fs.

The MOF output signal is significantly degraded and has a very low intensity (the maximum intensity is ≤ 1.15e-7). At the same time, duration of the NP output signal is 1.47 fs (absolute elongation is 0.68 fs; relative elongation is 86.1%) and the maximum intensity is

Optics EXPRESS

relatively high (approximately 0.86). This fact indicates that, in contrast with the MOF, the NP can be used to excite longitudinal vibrations in a sample.

3.3. Usual (regular) and tapered single-mode optical fibers

The issue of NP excitation is worth addressing here, as in order to obtain an undistorted output pulse at the apex of the NP, it is necessary to deliver an undistorted laser pulse to the input coupler of the NP. In the case of NP fabrication on the facet of an optical fiber [45] or in the case of NP excitation using the photoplastic connector [55], this delivery function lay on an optical fiber, either a usual (regular) or tapered one. It is thus important to understand how the input pulse is degraded during propagation through these structures [70].

Figure 13 illustrates the signal intensity envelopes at the start and end of a common single-mode optical fiber (core diameter is 4,000 nm; fiber length is 5,000 nm) for excitation laser pulse durations Δt of (a) 0.79 fs, (b) 4.33 fs, and (c) 9.45 fs. It should be noted here that the output signal intensities were renormalized according to the electric field anti-node at the point of the output signal measurement (the anti-node originates from the electromagnetic wave reflection at the fiber end facet as a result of the finite length of the fiber).

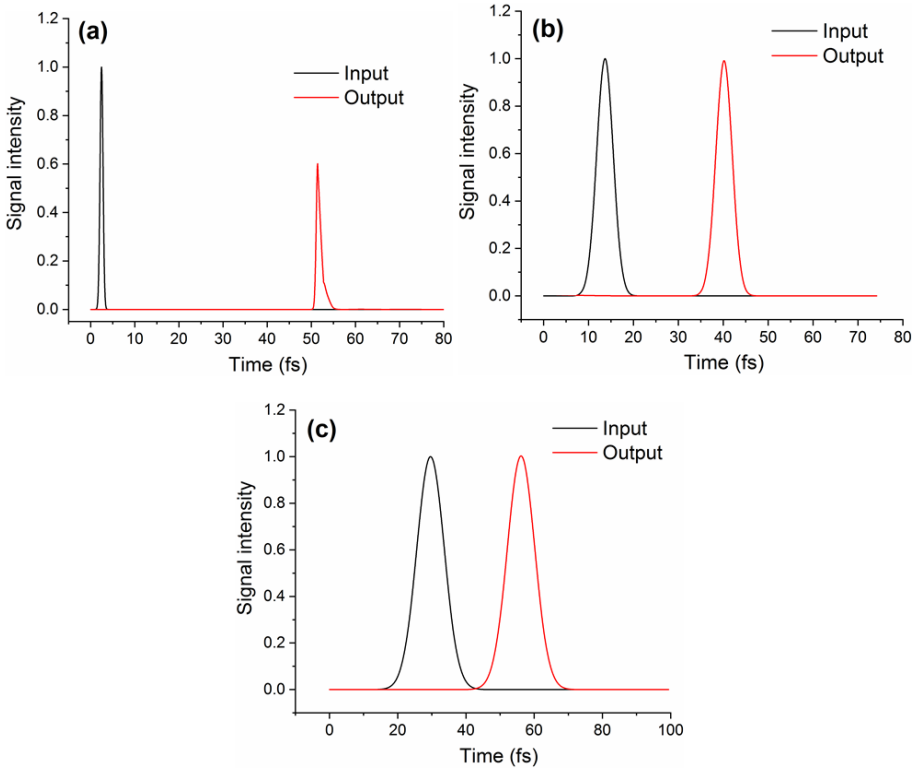

Fig. 13. Signal intensity envelopes at the start and end of the usual single-mode optical fiber for excitation laser pulse durations Δt of (a) 0.79 fs, (b) 4.33 fs, and (c) 9.45 fs.

From Fig. 13(a) {Δt = 0.79 fs}, the output signal peak intensity is 0.60. Local field reduction is 1.7 times. The duration of the output signal peak is 1.15 fs (absolute elongation is 0.36 fs; relative elongation is 45.6%). The time delay between the input signal peak and the peak of the output signal is 26.31 fs.

From Fig. 13(b) {Δt = 4.33 fs}, the output signal peak intensity is 0.992. Local field reduction is 1.008 times. The duration of the end peak is 4.31 fs (absolute compression is 0.02 fs; relative compression is 0.5%). The time delay between the input signal peak and the peak of the output signal is 26.31 fs.

Optics EXPRESS

From Fig. 13(c) {Δt = 9.45 fs}, the output signal peak intensity is 1.005. Local field enhancement is 1.005 times. The duration of the output signal peak is 9.44 fs (absolute compression is 0.01 fs; relative compression is 0.1%). The time delay between the input signal peak and the first peak of the output signal is 26.54 fs. In fact, the deviations in intensity and duration for Δt = 4.33 and 9.45 fs can be attributed to computational error, as they are negligibly small (≤ 0.5%).

From Figs. 13(a)–13(c), we can conclude that a common optical fiber does not lead to significant pulse elongations for pulses with duration $\Delta t \geq 4$ fs, for which the shape and duration are preserved virtually ideally. However, for very ultrashort pulses, i.e., < 1 fs, an optical fiber with a very wide bandwidth and low loss is required to obtain an undistorted output pulse [71].

Figure 14 shows the signal intensity (a) and intensity envelopes (b,c) at the start and end of a tapered single-mode optical fiber (start core diameter is 4,000 nm; end core diameter is 600 nm; taper length is 3,000 nm; convergence semi-angle α is 29.5°) for excitation laser pulse durations Δt of (a) 0.79 fs, (b) 4.33 fs, and (c) 9.45 fs.

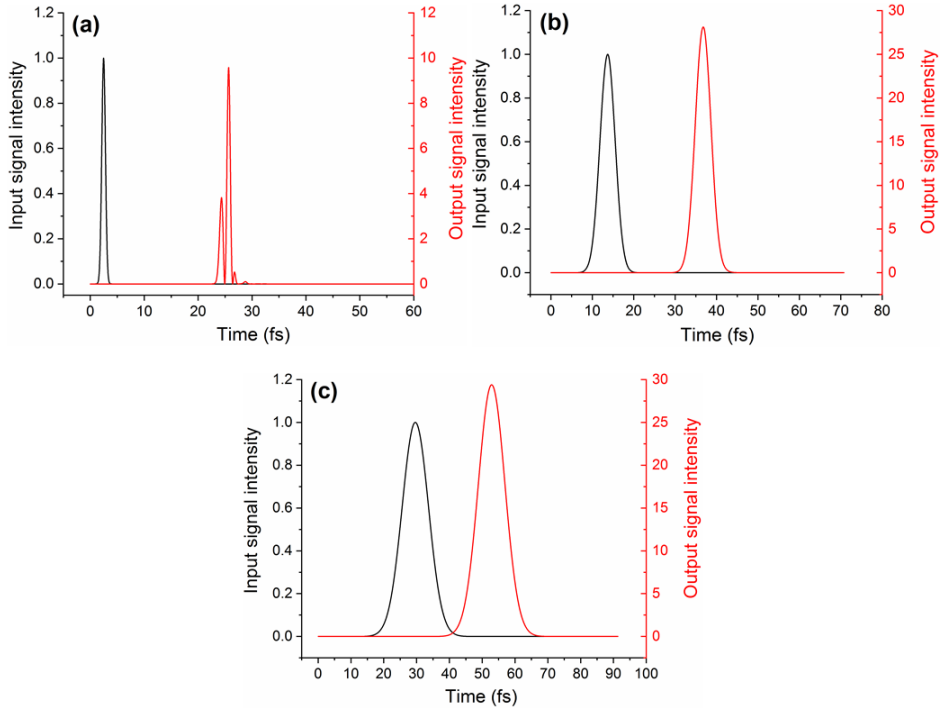

Fig. 14. Signal intensity (a) and intensity envelopes (b,c) at the start and end of a tapered single-mode optical fiber for excitation laser pulse durations Δt of (a) 0.79 fs, (b) 4.33 fs, and (c) 9.45 fs.

From Fig. 14(a) {Δt = 0.79 fs}, the local field enhancement is approximately 10 times. The output signal is slightly wider than the input signal.

From Fig. 14(b) {Δt = 4.33 fs}, the output signal peak intensity is 28.117. Local field enhancement is 28.1 times. The duration of the output signal peak is 4.46 fs (absolute elongation is 0.13 fs; relative elongation is 3.0%). The time delay between the input signal peak and the peak of the output signal is 23.08 fs.

From Fig. 14(c) {Δt = 9.45 fs}, the output signal peak intensity is 29.5. Local field enhancement is 29.5 times. The duration of the output signal peak is 9.53 fs (absolute elongation is 0.08 fs; relative elongation is 0.8%). The time delay between the input signal peak and the peak of the output signal is 23.25 fs.

Optics EXPRESS

Therefore, from Fig. 14, it is obvious that the output pulse of the tapered fiber undergoes barely noticeable degradation, even for very ultrashort input pulse duration (0.79 fs), and for pulses > 4 fs, it has virtually the same duration with an enhanced intensity (up to 30 times; this result coincides with the results obtained in [72]).

Figure 15 shows the signal intensities (not envelopes) at the start and end of a tapered single-mode optical fiber with shorter (1,000 nm; $\alpha = 59.5°$) and longer (5,000 nm; $\alpha = 18.8°$) tapers. From Fig. 15, it is clear that the output signal of this structure is sensitive to changes in the structure, so it requires preliminary engineering work before fabrication to obtain a set output pulse shape at the apex. However, detailed analysis of these structures (usual and tapered optical fibers) is beyond the scope of the current study.

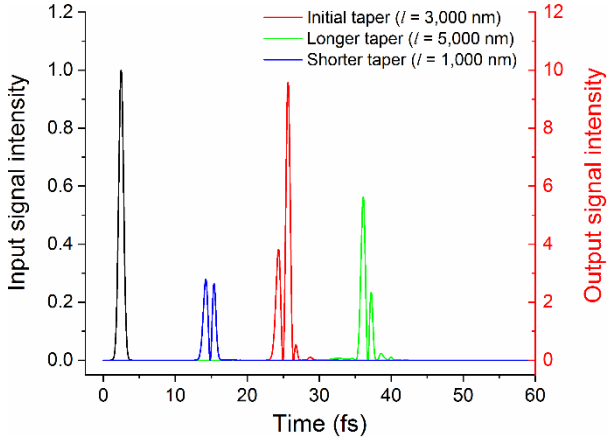

Fig. 15. Signal intensities (not envelopes) at the start and end of a tapered single-mode optical fiber with shorter (1,000 nm; $\alpha = 59.5°$) and longer (5,000 nm; $\alpha = 18.8°$) tapers.

4. Conclusion

In summary, we performed a computational experiment on ultrashort pulse propagation in tapered and metalized optical fibers (MOFs) and optical plasmon nanostrip probes (NPs). Numerical results showed that the temporal response at the apex of a MOF is severely distorted relative to the input pulse and the output signal is characterized by multiple peaks with different durations and intensities. The heaviest distortions were observed for the case of an input pulse with a duration of 0.79 fs (absolute and relative elongations of the output signal first peak are up to 2.07 fs and 262.0%, respectively). However, for input pulses with durations of 4.33 and 9.45 fs, distortions of the output signal are also marked: the absolute and relative elongations of the output signal first peak are up to 3.44 fs and 79.4%, respectively. This intensity peak elongation causes a significant drop in the field intensity for extremely short pulses at the probe apex and decreases the nonlinear interaction of light with a sample. Also, the axial z-component of the output signal of the MOF is very weak and distorted and cannot be used for longitudinal vibration excitation. Additionally, the temporal response at the MOF apex is critically sensitive to changes in the MOF parameters (such as convergence semi-angle and taper length) and cannot provide any significant local field enhancement. The spectral response is characterized by an irregular distribution resulting from the “cutoff effect” of the MOF.

Compared with the MOF, the NP provides a temporal response at its apex that virtually replicates the Gaussian shape and duration of the input pulse for input pulse durations of 4.33 and 9.45 fs (absolute and relative elongations are no more than 0.2 fs and 2.3%, respectively). At the same time, for an input pulse of $\Delta t = 0.79$ fs, a larger output pulse extension was observed (absolute and relative elongations of the output signal peak are up to 0.64 fs and 81.0%, respectively). However, even in this case, the output signal has only one peak, which

Optics EXPRESS

preserves the virtually ideal Gaussian shape. In addition, the output signal shape is insensitive to changes in the structure configuration for all pulse durations, which means it is easy for this structure to control the output signal, and it does not require any in-depth preliminary engineering work. Therefore, this structure does not require careful manufacturing with high reproducibility. The axial z-component of the NP output is also very intense and undistorted and therefore can be used to excite longitudinal vibrations in a sample. Analysis of the spectral response of the NP shows that the amplitude of the output signal is higher than that for the input signal throughout the entire frequency range. Additionally, the amplitude distribution is virtually uniform.

Propagation of fs pulses was also briefly analyzed for usual and tapered optical fibers. Taken together, these findings reveal the high potential of optical plasmon nanostrip probes as an ultrashort pulse delivery system to nanometer-size areas and make its usage very promising in a wide variety of techniques studying ultrafast processes in nanoscopic volumes. Along with the recently proposed methods of manufacture and effective excitation of the NP [45,55], we believe that the present study will provide a new impetus to the development of ultrafast nanophotonics.

Appendix. Mesh adaptation details and analysis of the convergence of numerical results

Mesh adaptation was performed using two parameters: flux of radiation through the control area, P_{apex} and the parameter, $S1,1$. Mesh adaptation was performed for initial laser pulse duration of 0.79 fs centered at 833 nm.

Model 1: Tapered and metalized optical fiber (MOF). Model 1 comprises a bare fused SiO_2 core entirely covered by Au coating (see Figure 1 of the main text). Parameters of the model 1 used for mesh adaptation process are as follows: l = 5,161 nm; α = 20.7°; d = 100 nm. The control area, P_{apex} has a circular shape and is located 25 nm before MOF tip apex. P_{apex} has a diameter of 600 nm. The magnetic wall was placed in the plane of symmetry, y = 0. Table 1 illustrates the radiant flux through the control area, values of the $S1,1$ and the corresponding relative errors, δ at a central frequency, f = 360 THz for different mesh cell numbers.

Table 1. Radiant flux through the control area, values of the $S1,1$ and the corresponding relative errors, δ at central frequency, f = 360 THz for different mesh cell numbers

Mesh cells	Minimum mesh step, nm	Maximum mesh step, nm	P_{apex}, a.u.	$\delta(P_{apex})$, %	$S1,1$, dB	$\delta(S1,1)$, %
82,809,216	5	24.963	0.0073492	43.415	–17.09694	4.125
96,208,250	5	23.6228	0.0073708	43.249	–17.06551	4.301
130,518,360	5	21.5482	0.012641	2.672	–17.88237	0.279
193,955,328	**5**	**18.3792**	**0.012988**	**0**	**-17.83253**	**0**

It can be seen from the presented data that the point with the maximum number of mesh cells can be taken as the reference value with a relative error of 0. In the study of model 1 the parameters in bold type in Table 1 were used. In Fig. 16, the dependence of the relative errors, δ on the mesh cell numbers is shown.

Optics EXPRESS

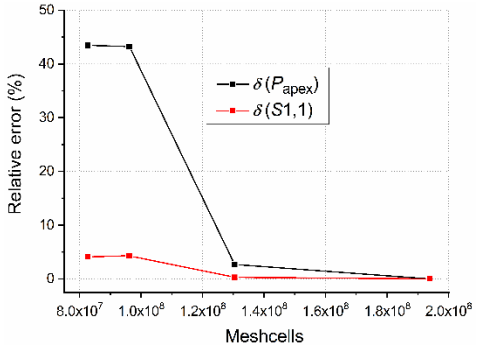

Fig. 16. Dependence of the relative errors, δ on the mesh cell numbers.

Model 2: Optical plasmon nanostrip probe (NP). Model 2 comprises a bare fused SiO_2 central layer with two (top and bottom) Au strips (see Fig. 2 of the main text). Parameters of the model 2 used for mesh adaptation process are as follows: l = 400 nm; α = 46.4°. The control area, P_{apex} has a rectangular shape and is located 25 nm before NP tip apex. P_{apex} has a size of 300 nm × 300 nm. The magnetic wall was placed in the plane of symmetry, y = 0. Table 2 shows the radiant flux through the control area, values of the $S1,1$ and the corresponding relative errors, δ at a central frequency, f = 360 THz for different mesh cell numbers.

Table 2. Radiant flux through the control area, values of the $S1,1$ and the corresponding relative errors, δ at central frequency, f = 360 THz for different mesh cell numbers

Mesh cells	Minimum mesh step, nm	Maximum mesh step, nm	P_{apex}, a.u.	$\delta(P_{apex})$, %	$S1,1$, dB	$\delta(S1,1)$, %
51,174,240	1	45.3333	0.040447	7.942	–5.8372	2.645
77,858,352	1	17.3491	0.037657	0.496	–5.70595	0.337
89,361,792	**1**	**14.8707**	**0.037558**	**0.232**	**-5.69455**	**0.137**
102,234,342	1	12.3868	0.037471	0	–5.68677	0

It can be seen from the presented data that the point with the maximum number of mesh cells can be taken as the reference value with a relative error of 0. In the study of model 2 the parameters in bold type in Table 2 were used. In the case, the relative error does not exceed 0.3 and 0.2% for the radiant flux and $S1,1$, respectively. In Fig. 17, the dependence of the relative errors, δ on the mesh cell numbers is illustrated.

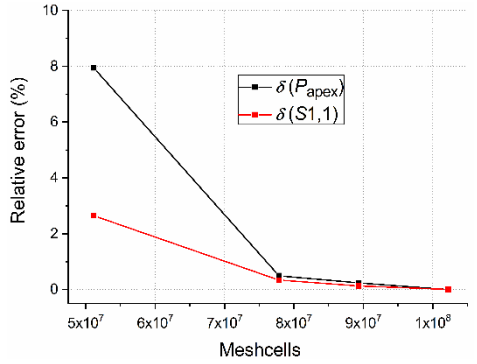

Fig. 17. Dependence of the relative errors, δ on the mesh cell numbers.

Model 3: Usual (regular) optical fiber. Model 3 comprises a bare fused SiO_2 core with a cladding made of the doped fused SiO_2 (2% lower refractive index). The core has a diameter

Optics EXPRESS

of 4,000 nm and the cladding has a diameter of 6,000 nm. The control area, P_{apex} has a circular shape and is located 25 nm before optical fiber end. P_{apex} has a diameter of 5,000 nm. The magnetic wall was placed in the plane of symmetry, $y = 0$. Table 3 illustrates the radiant flux through the control area, values of the $S1,1$ and the corresponding relative errors, δ at a central frequency, $f = 360$ THz for different mesh cell numbers. It can be seen from the presented data that the point with the maximum number of mesh cells can be taken as the reference value with a relative error of 0. In the study of model 3 the parameters in bold type in Table 3 were used. In the case, the relative error does not exceed 0.05 and 0.3% for the radiant flux and $S1,1$, respectively. In Fig. 18, the dependence of the relative errors, δ on the mesh cell numbers is shown.

Table 3. Radiant flux through the control area, values of the $S1,1$ and the corresponding relative errors, δ at central frequency, $f = 360$ THz for different mesh cell numbers

Mesh cells	Minimum mesh step, nm	Maximum mesh step, nm	P_{apex}, a.u.	$\delta(P_{apex})$, %	$S1,1$, dB	$\delta(S1,1)$, %
980,288	33.9807	65.7982	0.92376	2.573	–14.62828	9.236
21,697,642	13.1926	32.8947	0.94992	0.186	–13.23945	1.135
72,686,835	**8.78735**	**21.9298**	**0.94855**	**0.04**	**-13.42707**	**0.266**
154,169,730	8.77193	14.8707	0.94816	0	–13.39139	0

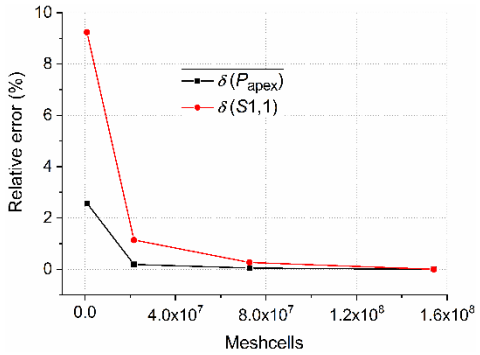

Fig. 18. Dependence of the relative errors, δ on the mesh cell numbers.

Model 4: Tapered optical fiber. Model 4 comprises a bare fused SiO_2 core with a cladding made of the doped fused SiO_2 (2% lower refractive index). The initial diameter of the core is 4,000 nm and of the cladding is 6,000 nm. The terminal diameter of the core is 600 nm and of the cladding is 700 nm. The convergence semi-angle α is 29.5°.The control area, P_{apex} has a circular shape and is located 100 nm before optical fiber end. P_{apex} has a diameter of 1,400 nm. The magnetic wall was placed in the plane of symmetry, $y = 0$. Table 4 shows the radiant flux through the control area, values of the $S1,1$ and the corresponding relative errors, δ at a central frequency, $f = 360$ THz for different mesh cell numbers.

It can be seen from the presented data that the point with the maximum number of mesh cells can be taken as the reference value with a relative error of 0. In the study of model 4 the parameters in bold type in Table 4 were used. In the case, the relative error does not exceed 0 for both radiant flux and $S1,1$. In Fig. 19, the dependence of the relative errors, δ on the mesh cell numbers is illustrated.

Optics EXPRESS

Table 4. Radiant flux through the control area, values of the $S1,1$ and the corresponding relative errors, δ at central frequency, $f = 360$ THz for different mesh cell numbers

Mesh cells	Minimum mesh step, nm	Maximum mesh step, nm	P_{apex}, a.u.	$\delta(P_{apex})$, %	$S1,1$, dB	$\delta(S1,1)$, %
14,526,784	2	75.3889	0.30041	5.156	–21.23657	3.589
25,442,784	2	49.9259	0.31307	1.159	–20.09722	1.969
40,150,074	2	37.1944	0.31507	0.572	–19.75468	3.640
58,601,604	2	29.5556	0.31572	0.322	–20.11875	1.864
82,961,400	**2**	**24.463**	**0.31674**	**0**	**-20.50087**	**0**

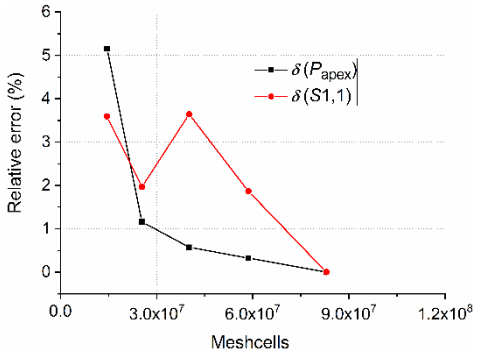

Fig. 19. Dependence of the relative errors, δ on the mesh cell numbers.

Funding

National Key R&D Program of China (2018YFB0504600, 2018YFB0504603); National Natural Science Foundation of China (NSFC) (61571399); Special Funding of "the Belt and Road" International Cooperation of Zhejiang Province (2015C04005); R&D Funding of the National Academy of Sciences of Ukraine (0119U001105).

References

1. C.-H. Liao, P. Wang, C. Y. Huang, P. Lin, G. Eakins, R. T. Bentley, R. Liang, and J.-X. Cheng, "In vivo and in situ spectroscopic imaging by a handheld stimulated Raman scattering microscope," ACS Photonics **5**(3), 947–954 (2018).
2. S. Huang, R. Pandey, I. Barman, J. Kong, and M. Dresselhaus, "Raman enhancement of blood constituent proteins using graphene," ACS Photonics **5**(8), 2978–2982 (2018).
3. D. Y. Usachov, V. Y. Davydov, V. S. Levitskii, V. O. Shevelev, D. Marchenko, B. V. Senkovskiy, O. Y. Vilkov, A. G. Rybkin, L. V. Yashina, E. V. Chulkov, I. Y. Sklyadneva, R. Heid, K.-P. Bohnen, C. Laubschat, and D. V. Vyalikh, "Raman spectroscopy of lattice-matched graphene on strongly interacting metal surfaces," ACS Nano **11**(6), 6336–6345 (2017).
4. S. Sil and S. Umapathy, "Raman spectroscopy explores molecular structural signatures of hidden materials in depth: universal multiple angle raman spectroscopy," Sci. Rep. **4**(1), 5308–5314 (2015).
5. N. Spegazzini, I. Barman, N. C. Dingari, R. Pandey, J. S. Soares, Y. Ozaki, and R. R. Dasari, "Spectroscopic approach for dynamic bioanalyte tracking with minimal concentration information," Sci. Rep. **4**(1), 7013–7019 (2015).
6. J. M. Zhang, M. Giehler, A. Göbel, T. Ruf, M. Cardona, E. E. Haller, and K. Itoh, "Optical phonons in isotopic Ge studied by Raman scattering," Phys. Rev. B Condens. Matter Mater. Phys. **57**(3), 1348–1351 (1998).
7. K. Chen, T. Wu, H. Wei, X. Wu, and Y. Li, "High spectral specificity of local chemical components characterization with multichannel shift-excitation Raman spectroscopy," Sci. Rep. **5**(1), 13952 (2015).
8. A. Cantarero, "Raman scattering applied to materials science," Procedia Mater. Sci. **9**, 113–122 (2015).
9. S. Wachsmann-Hogiu, T. Weeks, and T. Huser, "Chemical analysis in vivo and in vitro by Raman spectroscopy--from single cells to humans," Curr. Opin. Biotechnol. **20**(1), 63–73 (2009).
10. K. J. I. Ember, M. A. Hoeve, S. L. McAughtrie, M. S. Bergholt, B. J. Dwyer, M. M. Stevens, K. Faulds, S. J. Forbes, and C. J. Campbell, "Raman spectroscopy and regenerative medicine: a review," NPJ Regen. Med. **2**(1), 12 (2017).
11. B. Yu, M. Ge, P. Li, Q. Xie, and L. Yang, "Development of surface-enhanced Raman spectroscopy application for determination of illicit drugs: Towards a practical sensor," Talanta **191**, 1–10 (2019).

Optics EXPRESS

12. A. V. Tausenev, P. G. Kryukov, M. M. Bubnov, M. E. Likhachev, E. Y. Romanova, M. V. Yashkov, V. F. Khopin, and M. Y. Salganskii, "Efficient source of femtosecond pulses and its use for broadband supercontinuum generation," Quantum Electron. **35**(7), 581–585 (2005).
13. M. Wollenhaupt and T. Baumert, "Ultrafast laser control of electron dynamics in atoms, molecules and solids," Faraday Discuss. **153**, 9–26 (2011).
14. Y. Xu, X. Wei, Z. Ren, K. K. Y. Wong, and K. K. Tsia, "Ultrafast measurements of optical spectral coherence by single-shot time-stretch interferometry," Sci. Rep. **6**(1), 27937 (2016).
15. T. Kobayashi, "Development of ultrashort pulse lasers for ultrafast spectroscopy," Photonics **5**(3), 19 (2018).
16. L. Piatkowski, N. Accanto, and N. F. van Hulst, "Ultrafast meets ultrasmall: controlling nanoantennas and molecules," ACS Photonics **3**(8), 1401–1414 (2016).
17. D. Brinks, M. Castro-Lopez, R. Hildner, and N. F. van Hulst, "Plasmonic antennas as design elements for coherent ultrafast nanophotonics," Proc. Natl. Acad. Sci. U.S.A. **110**(46), 18386–18390 (2013).
18. V. Kravtsov, R. Ulbricht, J. M. Atkin, and M. B. Raschke, "Plasmonic nanofocused four-wave mixing for femtosecond near-field imaging," Nat. Nanotechnol. **11**(5), 459–464 (2016).
19. E. Mårsell, A. Losquin, R. Svärd, M. Miranda, C. Guo, A. Harth, E. Lorek, J. Mauritsson, C. L. Arnold, H. Xu, A. L'Huillier, and A. Mikkelsen, "Nanoscale imaging of local few-femtosecond near-field dynamics within a single plasmonic nanoantenna," Nano Lett. **15**(10), 6601–6608 (2015).
20. C. W. Ballmann, B. Cao, A. M. Sinyukov, A. V. Sokolov, and D. V. Voronine, "Dual-tip-enhanced ultrafast CARS nanoscopy," New J. Phys. **16**(8), 083004 (2014).
21. P. A. Golovinski, E. S. Manuylovich, and V. A. Astapenko, "Adiabatic description of superfocusing of femtosecond plasmon polaritons," J. Mod. Opt. **65**(8), 920–927 (2018).
22. S. Berweger, J. M. Atkin, X. G. Xu, R. L. Olmon, and M. B. Raschke, "Femtosecond nanofocusing with full optical waveform control," Nano Lett. **11**(10), 4309–4313 (2011).
23. V. Kravtsov, J. M. Atkin, and M. B. Raschke, "Group delay and dispersion in adiabatic plasmonic nanofocusing," Opt. Lett. **38**(8), 1322–1324 (2013).
24. S. Schmidt, B. Piglosiewicz, D. Sadiq, J. Shirdel, J. S. Lee, P. Vasa, N. Park, D. S. Kim, and C. Lienau, "Adiabatic nanofocusing on ultrasmooth single-crystalline gold tapers creates a 10-nm-sized light source with few-cycle time resolution," ACS Nano **6**(7), 6040–6048 (2012).
25. J. Vogelsang, J. Robin, B. J. Nagy, P. Dombi, D. Rosenkranz, M. Schiek, P. Groß, and C. Lienau, "Ultrafast electron emission from a sharp metal nanotaper driven by adiabatic nanofocusing of surface plasmons," Nano Lett. **15**(7), 4685–4691 (2015).
26. M. Müller, V. Kravtsov, A. Paarmann, M. B. Raschke, and R. Ernstorfer, "Nanofocused plasmon-driven sub-10 fs electron point source," ACS Photonics **3**(4), 611–619 (2016).
27. M. Zhang and T. Wang, "Plasmonic probe with circular nano-moat for far-field free nanofocusing," Nanoscale Res. Lett. **11**(1), 421 (2016).
28. P. Bazylewski, S. Ezugwu, and G. Fanchini, "A review of three-dimensional scanning near-field optical microscopy (3D-SNOM) and its applications in nanoscale light management," Appl. Sci. (Basel) **7**(10), 973 (2017).
29. B. Hecht, H. Bielefeldt, Y. Inouye, D. W. Pohl, and L. Novotny, "Facts and artifacts in near-field optical microscopy," J. Appl. Phys. **81**(6), 2492–2498 (1997).
30. Y. M. Morozov and A. S. Lapchuk, "Signal of microstrip scanning near-field optical microscope in far- and near-field zones," Appl. Opt. **55**(13), 3468–3477 (2016).
31. H. Harutyunyan, A. B. F. Martinson, D. Rosenmann, L. K. Khorashad, L. V. Besteiro, A. O. Govorov, and G. P. Wiederrecht, "Anomalous ultrafast dynamics of hot plasmonic electrons in nanostructures with hot spots," Nat. Nanotechnol. **10**(9), 770–774 (2015).
32. H. A. Huckabay, K. P. Armendariz, W. H. Newhart, S. M. Wildgen, and R. C. Dunn, "Near-field scanning optical microscopy for high-resolution membrane studies," Methods Mol. Biol. **950**, 373–394 (2013).
33. R. C. Dunn, "Near-field scanning optical microscopy," Chem. Rev. **99**(10), 2891–2928 (1999).
34. L. Sileo, M. Pisanello, A. Della Patria, M. S. Emhara, F. Pisanello, and M. De Vittorio, "Optical fiber technologies for in-vivo light delivery and optogenetics," *2015 17th International Conference on Transparent Optical Networks (ICTON)* (IEEE, 2015), pp. 1–5.
35. F. Pisano, M. Pisanello, L. Sileo, A. Qualtieri, B. L. Sabatini, M. De Vittorio, and F. Pisanello, "Focused ion beam nanomachining of tapered optical fibers for patterned light delivery," Microelectron. Eng. **195**, 41–49 (2018).
36. G. P. Agrawal, *Nonlinear Fiber Optics* (Academic Press, 2013).
37. L. Novotny and C. Hafner, "Light propagation in a cylindrical waveguide with a complex, metallic, dielectric function," Phys. Rev. E Stat. Phys. Plasmas Fluids Relat. Interdiscip. Topics **50**(5), 4094–4106 (1994).
38. U. Schröter and A. Dereux, "Surface plasmon polaritons on metal cylinders with dielectric core," Phys. Rev. B Condens. Matter Mater. Phys. **64**(12), 125420 (2001).
39. A. S. Lapchuk, "Estimation of optical efficiency of a near-field optical microscope on the basis of a simplified mathematical model," J. Opt. A: Pure Appl. Opt. **3**(6), 455–459 (2001).
40. A. S. Lapchuk, D. Shin, H.-S. Jeong, C. S. Kyong, and D.-I. Shin, "Mode propagation in optical nanowaveguides with dielectric cores and surrounding metal layers," Appl. Opt. **44**(35), 7522–7531 (2005).
41. J. Conway, *Efficient Optical Coupling to the Nanoscale*, Ph.D. thesis, University of California, 2006.

Optics EXPRESS

42. A. S. Lapchuk, S.-K. Yun, V. Yurlov, J.-H. Song, S. An, and I. Nevirkovets, "Numerical simulation of characteristics of near-field microstrip probe having pyramidal shape," J. Opt. Soc. Am. A **24**(8), 2407–2417 (2007).
43. H. Choo, M.-K. Kim, M. Staffaroni, T. J. Seok, J. Bokor, S. Cabrini, P. J. Schuck, M. C. Wu, and E. Yablonovitch, "Nanofocusing in metal-insulator-metal gap plasmon waveguide with a three-dimensional linear taper," Nat. Photonics **6**, 838–844 (2012).
44. W. Bao, M. Staffaroni, J. Bokor, M. B. Salmeron, E. Yablonovitch, S. Cabrini, A. Weber-Bargioni, and P. J. Schuck, "Plasmonic near-field probes: a comparison of the campanile geometry with other sharp tips," Opt. Express **21**(7), 8166–8176 (2013).
45. G. Calafiore, A. Koshelev, T. P. Darlington, N. J. Borys, M. Melli, A. Polyakov, G. Cantarella, F. I. Allen, P. Lum, E. Wong, S. Sassolini, A. Weber-Bargioni, P. J. Schuck, S. Cabrini, and K. Munechika, "Campanile near-field probes fabricated by nanoimprint lithography on the facet of an optical fiber," Sci. Rep. **7**(1), 1651 (2017).
46. P. Kukura, D. W. McCamant, and R. A. Mathies, "Femtosecond stimulated Raman spectroscopy," Annu. Rev. Phys. Chem. **58**(1), 461–488 (2007).
47. M. N. Ashner and W. A. Tisdale, "High repetition-rate femtosecond stimulated Raman spectroscopy with fast acquisition," Opt. Express **26**(14), 18331–18340 (2018).
48. D. R. Dietze and R. A. Mathies, "Femtosecond stimulated Raman spectroscopy," ChemPhysChem **17**(9), 1224–1251 (2016).
49. S. M. Hart, W. R. Silva, and R. R. Frontiera, "Femtosecond stimulated Raman evidence for charge-transfer character in pentacene singlet fission," Chem. Sci. (Camb.) **9**(5), 1242–1250 (2018).
50. M. Kloz, R. Grondelle, and J. Kennis, "Femtosecond stimulated Raman spectroscopy in 1D and 2D – direct observation of intramolecular motions and intermolecular interactions," *2013 Conference on Lasers & Electro-Optics Europe & International Quantum Electronics Conference CLEO EUROPE/IQEC* (IEEE, 2013).
51. B. P. Molesky, Z. Guo, and A. M. Moran, "Femtosecond stimulated Raman spectroscopy by six-wave mixing," J. Chem. Phys. **142**(21), 212405 (2015).
52. B. Zhao, K. Niu, X. Li, and S.-Y. Lee, "Simple aspects of femtosecond stimulated Raman spectroscopy," Sci. China Chem. **54**(12), 1989–2008 (2011).
53. H. Kuramochi, S. Takeuchi, and T. Tahara, "Femtosecond time-resolved impulsive stimulated Raman spectroscopy using sub-7-fs pulses: apparatus and applications," Rev. Sci. Instrum. **87**(4), 043107 (2016).
54. S. Fujiyoshi, S. Takeuchi, and T. Tahara, "Time-resolved impulsive stimulated Raman scattering from excited-state polyatomic molecules in solution," J. Phys. Chem. A **107**(4), 494–500 (2003).
55. Y. M. Morozov, A. S. Lapchuk, M.-L. Fu, A. A. Kryuchyn, H.-R. Huang, and Z.-C. Le, "Numerical analysis of end-fire coupling of surface plasmon polaritons in a metal-insulator-metal waveguide using a simple photoplastic connector," Photon. Res. **6**(3), 149–156 (2018).
56. A. Taflove and S. C. Hagness, *Computational Electrodynamics: the Finite-Difference Time-Domain Method* (Artech House, 2010).
57. C. F. Bohren and D. R. Huffman, *Absorption and Scattering of Light by Small Particles* (Wiley-VCH, 2009).
58. E. D. Palik, *Handbook of Optical Constants of Solids* (Academic Press, 1985).
59. FDTD Solutions, Lumerical Solutions, Inc., Vancouver, Canada.
60. D. Fisher, M. Fraenkel, Z. Henis, E. Moshe, and S. Eliezer, "Interband and intraband (Drude) contributions to femtosecond laser absorption in aluminum," Phys. Rev. E Stat. Nonlin. Soft Matter Phys. **65**(1 Pt 2), 016409 (2002).
61. X. Zhang, C. Huang, M. Wang, P. Huang, X. He, and Z. Wei, "Transient localized surface plasmon induced by femtosecond interband excitation in gold nanoparticles," Sci. Rep. **8**(1), 10499 (2018).
62. J. A. Veerman, A. M. Otter, L. Kuipers, and N. F. van Hulst, "High definition aperture probes for near-field optical microscopy fabricated by focused ion beam milling," Appl. Phys. Lett. **72**(24), 3115–3117 (1998).
63. S. Patanè, E. Cefalì, A. Arena, P. G. Gucciardi, and M. Allegrini, "Wide angle near-field optical probes by reverse tube etching," Ultramicroscopy **106**(6), 475–479 (2006).
64. J. Luo, Y. Fan, H. Zhou, W. Gu, and W. Xu, "Fabrication of different fine fiber tips for near field scanning optical microscopy by a simple chemical etching technique," Chin. Opt. Lett. **5**(S1), 232–234 (2007).
65. R. Stöckle, C. Fokas, V. Deckert, R. Zenobi, B. Sick, B. Hecht, and U. P. Wild, "High-quality near-field optical probes by tube etching," Appl. Phys. Lett. **75**(2), 160–162 (1999).
66. D. Pozar, *Microwave Engineering* (Wiley, 2012).
67. J. S. Huang, D. V. Voronine, P. Tuchscherer, T. Brixner, and B. Hecht, "Deterministic spatiotemporal control of optical fields in nanoantennas and plasmonic circuits," Phys. Rev. B Condens. Matter Mater. Phys. **79**(19), 195441 (2009).
68. M. Tsang, D. Psaltis, and F. G. Omenetto, "Reverse propagation of femtosecond pulses in optical fibers," Opt. Lett. **28**(20), 1873–1875 (2003).
69. A. M. Weiner, "Ultrafast optical pulse shaping: a tutorial review," Opt. Commun. **284**(15), 3669–3692 (2011).
70. D. Kim, H. Choi, S. Yazdanfar, and P. T. So, "Ultrafast optical pulse delivery with fibers for nonlinear microscopy," Microsc. Res. Tech. **71**(12), 887–896 (2008).
71. D. Marcuse, *Light Transmission Optics* (Van Nostrand Reinhold Company, 1982).
72. P. Savaliya and A. Dhawan, "Tapered fiber nanoprobes: plasmonic nanopillars on tapered optical fiber tips for large EM enhancement," Opt. Lett. **41**(19), 4582–4585 (2016).

138.68.231.97 {ts '2019-04-24 15:40:34'}